Volumetric B_1^+ Mapping of the Brain at 7T Using DREAM

Kay Nehrke,[1]* Maarten J. Versluis,[2] Andrew Webb,[2] and Peter Börnert[1,2]

Purpose: To tailor and optimize the Dual Refocusing Echo Acquisition Mode (DREAM) approach for volumetric B_1^+ mapping of the brain at 7T.
Theory and Methods: A new DREAM echo timing scheme based on the virtual stimulated echo was derived to minimize potential effects of transverse relaxation. Furthermore, the DREAM B_1^+ mapping performance was investigated in simulations and experimentally in phantoms and volunteers for volumetric applications, studying and optimizing the accuracy of the sequence with respect to saturation effects, slice profile imperfections, and T_1 and T_2 relaxation. Volumetric brain protocols were compiled for different isotropic resolutions (5–2.5 mm) and SENSE factors, and were studied in vivo for different RF drive modes (circular/linear polarization) and the application of dielectric pads.
Results: Volumetric B_1^+ maps with good SNR at 2.5 mm isotropic resolution were acquired in about 20 s or less. The specific absorption rate was well below the safety limits for all scans. Mild flow artefacts were observed in the large vessels. Moreover, a slight contrast in the ventricle was observed in the B_1^+ maps, which could be attributed to T_1 and T_2 relaxation effects.
Conclusion: DREAM enables safe, very fast, and robust volumetric B_1^+ mapping of the brain at ultrahigh fields. **Magn Reson Med 71:246–256, 2014.** © 2013 Wiley Periodicals, Inc.

Key words: B_1 mapping; B_0 mapping; RF shimming; high-field MRI; brain MRI; parallel transmission

Magnetic Resonance Imaging (MRI) at ultrahigh field strength ($\geq$7T) is promising for a variety of clinical applications in the brain (1) due to the improved intrinsic signal-to-noise (SNR) and susceptibility-induced contrast. However, there are also serious technical challenges, in particular transmit field non-uniformities and specific absorption rate (SAR) limitations. The inhomogeneous transmit fields, caused by wave propagation effects, affect the image contrast, and hence may compromise clinical diagnosis substantially. All approaches to counteract these effects, such as tailored RF pulses (2) or parallel transmit techniques [RF shimming (3,4) and transmit SENSE (5,6)], require knowledge about the actual B_1^+ fields involved. Also correction methods that are applied retrospectively, especially in quantitative imaging and spectroscopy applications, often require the knowledge about the actual B_1^+ to correct the corresponding bias (7). Moreover, measured B_1^+ maps may be used to determine electric tissue parameters and electric field components (8), potentially providing new diagnostic information. Furthermore, the SAR may be predicted in a patient-specific manner using measured B_1^+ map information (9), which can be interesting for the improvement of patient safety for ultra-high field imaging.

However, most established B_1^+ mapping approaches, either encoding the B_1^+ into the magnitude (10–24) or phase (25,26) of the measured signal, are relatively slow because of the frequent repetition of the B_1^+ encoding process and the need for at least two separate measurements for B_1^+ fitting. Especially at ultrahigh fields, the typically SAR-intense RF pulses required for B_1^+ encoding may limit the acquisition speed.

Recently, the DREAM (Dual Refocusing Echo Acquisition Mode) B_1^+ mapping approach was introduced (27), which is based on a STEAM preparation sequence (28) for B_1^+ encoding and a fast low-angle imaging pulse train for spatial encoding. Similar to other magnetization-prepared B_1^+ mapping approaches (12,22–24), this results in very low SAR values. Moreover, in contrast to existing techniques, the DREAM approach determines B_1^+ from a single acquisition only, measuring a free induction decay (FID) and a stimulated echo (STE) quasisimultaneously. Hence, the acquisition of a 2D B_1^+ map takes only a fraction of a second, which is at least an order of magnitude faster than most existing approaches.

Due to its high speed and low SAR burden, the DREAM approach represents an interesting candidate for B_1^+ mapping at ultrahigh fields. In the present work, the performance of DREAM for fast volumetric B_1^+ mapping of the brain at 7T is studied. For this purpose, volumetric B_1^+ mapping protocols based on DREAM are compiled for different resolutions and optimized in simulations and in experiments on phantoms and in vivo including also the use of parallel imaging. Moreover, a new DREAM sequence option based on the virtual stimulated echo is introduced, compensating the sequence for T_2 relaxation.

THEORY

Basic Sequence

The DREAM approach employs a STEAM magnetization preparation sequence consisting of two RF pulses of equal shape and flip angle α, followed by a low-angle imaging train, where both the STE and the FID signals are measured quasi-simultaneously as gradient-recalled echoes (27). The unknown flip angle α of the STEAM

pulses is derived from the ratio of the measured STE and FID signal magnitudes according to the simple analytic expression:

$$\alpha = \arctan \sqrt{2I_{STE}/I_{FID}} \qquad [1]$$

Figure 1 shows the schematic of the DREAM sequence for three different echo options used in this work. The so-called "FID first" and "STE first" options (cf. Fig. 1a,b) both employ the timing scheme:

$$T_S = TE_{STE} + TE_{FID} \qquad [2]$$

where T_S denotes the STEAM preparation pulse interval, and TE_{STE} and TE_{FID} denote the gradient echo times of the STE and FID signals, respectively. Thus, the STE will not fully rephase at the gradient echo time TE_{STE}, but will have a spectral encoding time $-TE_{FID}$. Therefore, STE and FID signals will have the same T_2^*-weighting, and Eq. [1] yields a T_2^*-compensated B_1^+ map. However, as a consequence of the T_2^*-compensation according to Eq. [2], the T_2-evolution times of the STE and FID signals differ by a time interval (27),

$$\Delta T_{T2} = 2TE_{STE} \qquad [3]$$

which may lead to a slight T_2-artifact in the B_1^+ map.

In contrast, the novel, third sequence option (cf. Fig. 1c), dubbed "STE* first", measures the so-called virtual stimulated echo (STE*), which represents the complex–conjugated counterpart of the STE (29). In contrast to the STE, the STE* is further dephasing after rotating the longitudinal magnetization into the transverse plane by the application of the imaging RF pulse β. Consequently, the STE* can simply be measured by employing the "STE first" option with inverted polarity of the STEAM dephaser gradient G_{m2} [see the extended-phase graph (30) in Fig. 1]. Moreover, both the spectral encoding time and the T_2 evolution time are identical for STE* and FID, namely TE_{FID}, provided the timing scheme obeys:

$$T_S = TE_{FID} - TE_{STE*} \qquad [4]$$

Then, a T_2- and T_2^*-compensated B_1^+ map may be derived from:

$$\alpha = \arctan \sqrt{2I_{STE*}/I_{FID}} \qquad [5]$$

METHODS

Numerical Simulations

During the DREAM imaging pulse train, T_1 relaxation results in a decay of the STEAM-prepared part of the longitudinal magnetization and a recovery of the unprepared longitudinal magnetization. Moreover, the imaging RF pulse train itself potentially leads to an exhausting of the longitudinal magnetization components and to
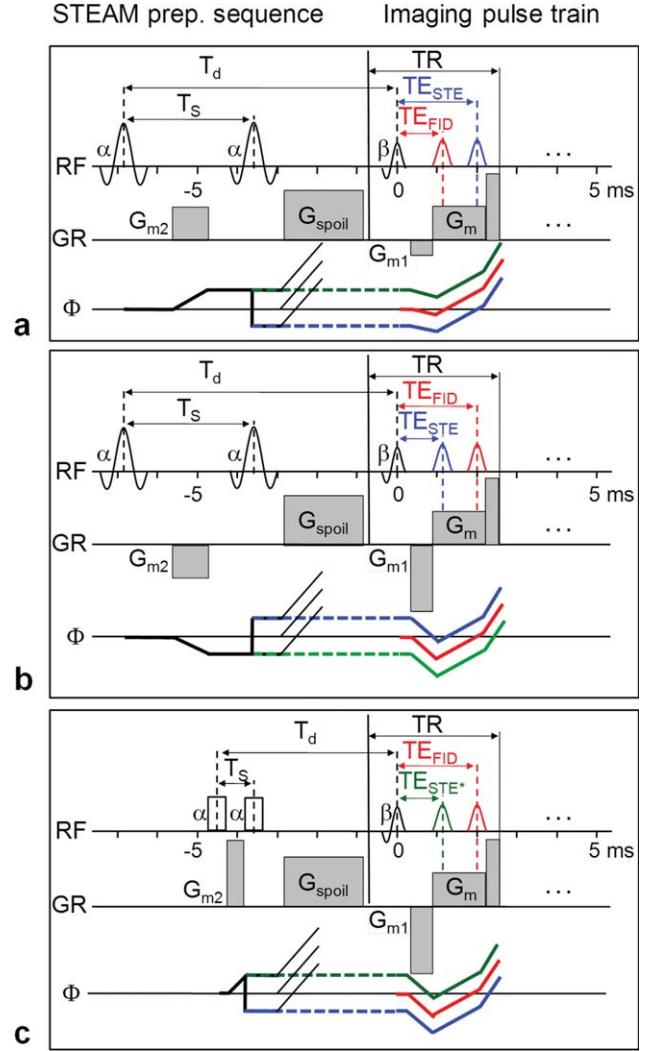

FIG. 1. DREAM pulse sequence scheme. The basic sequence consists of a STEAM magnetization preparation sequence (left), separated by an effective time delay T_d from a low-angle single shot imaging sequence (right, only one TR is shown). The imaging RF pulse β creates a STE (marked blue), a STE* (virtual stimulated echo, marked green), and an FID (marked red), which can be measured as separate gradient-recalled echoes. This is illustrated by the extended-phase graph Φ of the switched gradients (neglecting static off-resonance effects), where the solid and dashed lines represent transverse and longitudinal magnetization components, respectively. Echoes are formed where the solid lines cross $\Phi = 0$. The corresponding echo times TE_{STE} and TE_{FID} are adjusted by the area and polarity of the gradients G_m, G_{m1}, and G_{m2}. Three sequence options are shown—[a: $T_S = TE_{STE} + TE_{FID}$ and $TE_{STE} > TE_{FID}$ (FID first), b: $T_S = TE_{STE} + TE_{FID}$ and $TE_{STE} < TE_{FID}$ (STE first), c: $T_S = TE_{FID} - TE_{STE*}$ and $TE_{STE*} < TE_{FID}$ (STE* first), see Theory section for details]. Options (a) and (b) equalize T_2^* effects for STE and FID gradient echoes, while option (c) equalizes both T_2^* and T_2 effects for STE* and FID gradient echoes. The chosen time scale and the relative gradient areas are realistic and the echo times of about 1 and 2 ms lead to fat/water in-phase at 7 T for all sequence options. Note that for the "STE* first" option (c) block pulses were used for α to allow the selected short echo times. The gradient G_{spoil} is used for spoiling of spurious transverse magnetization (see extended-phase graph) and could also be applied in the slice-selection or phase-encoding direction. For clarity, the employed slice-selection and phase-encoding gradients have been omitted in this diagram.

additional contributions from higher order coherences (echoes). The k-space weighting resulting from these effects may impair the accuracy of the DREAM B_1^+ encoding principle (cf. Eq. [1]). Nevertheless, the approach is still based on the idealized picture that this weighting may be neglected for a centric phase encoding order. To study the validity of this assumption, numerical simulations on the accuracy of the method were performed for various sequence and tissue parameters. A custom Java algorithm was employed to track the contributions from all coherence pathways to the STE and FID signals during a DREAM shot according to configuration theory (29,30). Thus, echo train weighting functions were determined for both STE and FID signals. In a first step, spatial encoding was omitted and the flip angle α was predicted from a pair of STE and FID signals as a function of the echo number in the pulse train. In a second step, a spatial profile mimicking a simple rectangular object (size = 75% of field-of-view (FOV)) was considered, corresponding to a rectangular proton density function. To synthesize one dimensional (1D) STE and FID images, the profile was Fourier transformed to k-space, and appropriate weights were applied for STE and FID echoes according to the echo number in the pulse train. Finally, the resulting profiles were transformed back to image space and a 1D flip angle map was determined from the ratio of the profiles according to Eq. [3]. For simplicity and conciseness, a spatially homogeneous B_1^+ field was considered and the impact of noise was neglected. The simulations were performed for a typical DREAM protocol (number of echoes = 40, TR = 4 ms, delay between STEAM preparation and first imaging pulse $T_d = 8$ ms, centric phase encoding order), various actual flip angles ($\alpha = 25°$ to $75°$, $\beta = 5°$–$25°$), various T_1 values ($T_1 = 200$ ms to 1000 ms) and a fixed T_2 value ($T_2 = 100$ ms) while RF spoiling in the β pulse read-out train was omitted.

MRI System and RF Coils

A 7T whole body research MRI scanner (Achieva Platform, Philips Healthcare, Cleveland, USA) equipped with a quadrature Tx/Rx and 32-channel receive array head coil (Nova Medical) was used. For channel combination, SENSE (31) was applied using the quadrature Rx coil as reference.

DREAM Sequence Implementation

The DREAM sequence as previously described (27) and supplemented by the "STE* first" sequence option and an online DREAM B_1^+ map reconstruction on the scanner was implemented. The implementation allows the acquisition of B_1^+ maps in single-shot and multi-shot mode, as well. To minimize the T_1-related k-space weighting discussed above, a centric phase encoding order without startup echoes was used for the image acquisition pulse train. The impact of the phase encoding order on the accuracy of the method was also studied by phantom experiments (see below).

As previously described (27), both STEAM and image slice selection was based on standard sinc-gaussian-shaped RF pulses provided by the pulse library of the

scan software (cf. Fig. 1). The RF excitation pulse β chosen for imaging had a single side lobe preceding the main lobe, resulting in a pulse duration of 0.7 ms for a typical nominal flip angle of $10°$ and a nominal peak B_1 of 2.9 μT. The slice-selective STEAM pulses (α) chosen for volumetric B_1^+ mapping had one side lobe on each side of the main lobe, resulting in a pulse duration of 0.7 ms for a typical nominal flip angle of $40°$ and a nominal peak B_1 of 15 μT. For comparison, slice-selective STEAM pulses with Gaussian shape were applied in selected experiments, resulting in a pulse duration of 0.3 ms for a typical nominal flip angle of $40°$ and a nominal peak B_1 of 15 μT. In the case of single slice B_1^+ mapping, nonselective block pulses were used for the STEAM preparation sequence, resulting in a pulse duration of 0.2 ms for a typical nominal flip angle of $40°$ and a nominal peak B_1 of 15 μT. The nominal value of the flip angle α was preadjusted to align the expected spatial flip angle variation to the working range of the DREAM method (27).

The high peak B_1 of 15 μT was chosen to increase the flexibility of the sequence timing, particularly regarding the "STE* first" option (cf. Fig. 1c). The resulting head SAR of the overall sequence was typically about 40% of the safety limits (see detailed scan protocols indicated below). For the standard sequence options (i.e. "STE first" and "FID first") the peak B_1 may be reduced by about a factor of two without increasing the STEAM RF pulse interval T_S, resulting in SAR values of about 20%.

A constant STEAM flip angle α across the area affected by the slice selective excitation pulse β is crucial for the accuracy of the B_1^+ estimation according to Eq. [1]. Therefore, to account for slice profile imperfections in multislice acquisitions, the STEAM slice thickness was chosen larger than the image slice thickness (22,23,27), using a ratio $r = 2$ as the default. Hence, to avoid saturation effects resulting from the overlapping STEAM excitation profiles, the slices were acquired in an interleaved ("first odd, then even") fashion to allow for sufficient T_1 relaxation between the acquisition of adjacent slices. The robustness of this spatiotemporal slice acquisition scheme was studied in phantom experiments (see below).

Phantom Experiments

Phantoms with different dielectric properties and relaxation times were employed to study and optimize the robustness and accuracy of the DREAM sequence by adjusting various sequence parameters. A single-slice protocol was used as a template (transverse orientation, FOV = 320 × 190 mm^2, scan matrix = 128 × 77, phase-encoding direction: left-right, slice thickness = 5 mm, STEAM flip angle $\alpha = 40°$, imaging flip angle $\beta = 7°$, imaging sequence repetition time TR = 3.3 ms, echo times = 1.2/1.9 ms, echo order: STE first, STEAM RF pulse interval $T_S = 3.1$ ms, single shot duration = 250 ms, phase encoding order = centric).

A first set of phantom experiments was performed on an oil phantom (bottle, ø = 130 mm, filled with white mineral oil) to study the general accuracy of the method. A series of single-slice DREAM B_1^+ maps was measured for different STEAM flip angles ($\alpha = 5°$ to $90°$ in steps of

5°). The mean flip angle and its standard deviation was determined from a rectangular region of interest (ROI) (10 × 10 pixel) of the B_1^+ maps and compared to the nominal flip angle. The latter one was adjusted by the transmit gain calibration of the system, which was considered as accurate external reference for the chosen oil phantom and the accordingly expected spatially homogeneous transmit field.

A second set of phantom experiments was performed on a water sphere (ø = 140 mm, filled with salt-doped tap water), yielding a T_1 similar to that of cerebrospinal fluid (CSF, $T_1 \approx 3000$ ms), to study the robustness of the sequence against saturation effects. For this purpose, single-slice DREAM B_1^+ maps were measured after a dynamic series of dummy DREAM shots. The experiment was repeated for different shot intervals in the range 0.5–10.0 s and different nominal STEAM flip angles. The predicted flip angles were compared for a fixed pixel in the centre of the phantom. The B_1^+ maps, acquired after full relaxation (i.e. 10 s shot interval), were considered as accurate reference and the slope between predicted and nominal flip angles was used as a global scale factor for calibration of the remaining measurements of the series.

A third set of experiments was performed on the same phantom to check the impact of the STEAM slice profile imperfections on the accuracy of the method. For different nominal STEAM flip angles, the STEAM/imaging slice thickness ratio r was varied in the range 1.0–4.0 and the predicted flip angles were compared to the reference flip angles for a fixed pixel in the centre of the phantom. For comparison, additional experiments were performed with Gaussian shaped STEAM RF pulses instead of the sinc-gaussian pulses used as standard. The reference flip angles were derived from additional calibration experiments using non-selective block pulses for STEAM magnetization preparation.

A fourth set of experiments was performed to study the impact of T_1 relaxation during the image pulse train on the accuracy of the DREAM approach. This effect is expected to be more severe for short T_1. Therefore, a Gd-doped spectroscopy sphere phantom (ø = 170 mm) with moderate T_1 was chosen ($T_1 \approx 1000$ ms), which is significantly shorter than the T_1 of gray and white matter at 7T. 2D DREAM B_1^+ maps were acquired for different phase encoding orders (centric and linear) and different SENSE factors (1–4), which resulted in acquisition train lengths between 70 and 250 ms. The nominal STEAM flip angle was pre-calibrated to obtain a reference angle of about 60° in the centre of the phantom, which was used for evaluation.

Finally, a last set of phantom experiments was performed to study the T_2 weighting of the different echo timing schemes discussed in the Theory section. For this purpose, a rubber phantom [T_2^*, $T_2 \approx 1$ ms, (32)] was used. B_1^+ maps were acquired for three different echo timing schemes (FID first: TE = 0.88/1.72 ms, T_S = 2.6 ms; STE first: TE=1.11/1.95 ms, T_S= 3.06 ms; and STE* first: TE=1.11/1.95 ms, T_S= 0.84 ms). The timing schemes are fully T_2^*-compensated, but have T_2 evolution time differences between STE $^{(*)}$ and FID of 3.44, 2.22 and 0 ms, respectively (cf. Eqs. [2] and [3]). For

selected pixels in the map, the predicted flip angles were compared to the reference angle ($\alpha = 60^{\circ}$), which was adjusted by a calibration measurement on an oil phantom.

In Vivo Experiments

DREAM B_1^+ maps of the brain were acquired in nine healthy volunteers (one female, eight male, age: 24–52 years). Written consent was obtained according to the rules of the institution. All B_1^+ maps were acquired in single-shot mode using centric phase encoding order.

As a first set of experiments, volumetric B_1^+ maps were acquired (transverse orientation, FOV = 320 × 190 × 300 mm^3 (AP×LR×FH), phase-encoding direction: left-right, imaging flip angle $\beta = 7^{\circ}$, STEAM flip angle α= 40°, pixel bandwidth = 1250 Hz, "FID first" echo order, STEAM/imaging slice thickness ratio $r = 2$). Three protocols providing different isotropic resolutions were compared: (a) resolution = 5 mm, SENSE factor = 1, scan matrix= 64 × 38, slices = 60, echo times= 1.1/2.1 ms, TR= 3.4 ms, shot duration = 135 ms, total scan time = 8.1 s, head SAR < 1.4 W/kg (< 43%), (b) resolution = 3.3 mm, SENSE factor = 2, scan matrix= 96 × 31, slices = 96, echo times= 1.2/2.2 ms, TR= 3.6 ms, shot duration = 111 ms, total scan time = 9.9 s, head SAR < 1.5 W/kg (< 47%), (c) resolution = 2.5 mm, SENSE factor = 2, scan matrix= 128 × 41, slices = 120, echo times= 1.4/2.4 ms, TR= 3.8 ms, shot duration = 155 ms, total scan time= = 21.5 s, head SAR < 1.1 W/kg (< 35%). Note that for the 5 mm protocol (a) no scan acceleration by parallel imaging was applied (i.e. SENSE factor = 1) to avoid potential saturation effects between odd and even slices. Thus, the acquisition time delay between neighboring, overlapping slices was (a) 4 s, (b) 5 s and (c) 10.8 s.

The B_1^+ maps were reformatted according to the three orthogonal views and compared with respect to resolution, SNR and potential artifacts. Moreover, B_0 and transceive chain phase maps were derived from the phases of the STE and FID signals (27), applying a 2D unwrapping algorithm (33). The frequency offset f was derived from the phase φ of the unwrapped B_0 phase map according to:

$$f = \frac{\varphi}{2\pi}(2\text{TE}_{\text{FID}})^{-1} \qquad [6]$$

Furthermore, volumetric B_1^+ maps were acquired and compared for different RF excitation conditions. Thus, experiments with external dielectric pads filled with $BaTiO_3$ + deuterated water (34,35) placed near the head were performed, using the volumetric protocol with 3.3 mm isotropic resolution described above. Finally, B_1^+ maps were acquired separately for the two linearly polarized modes of the transmit coil using the protocol with 2.5 mm isotropic resolution indicated above. The B_1^+ maps were reformatted according to the three orthogonal views and compared to corresponding B_1^+ maps acquired with standard quadrature excitation.

As a further set of experiments, single-slice B_1^+ maps through the ventricle of the brain were acquired to check the robustness of the sequence with respect to the
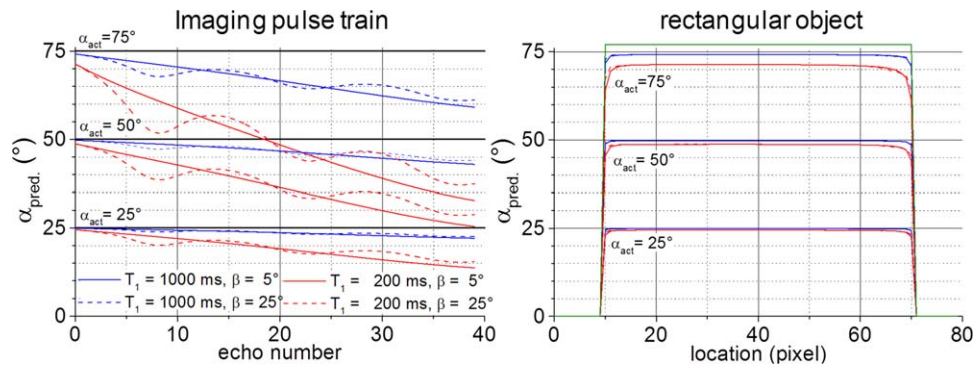
FIG. 2. DREAM B_1^+ mapping accuracy (simulations). Graph (a) shows the predicted STEAM flip angle as a function of the echo number in the pulse train for different actual STEAM flip angles, T_1 values and imaging flip angles β. The accuracy degrades with increasing echo number due to T_1 relaxation. Graph (b) shows the corresponding spatially resolved flip angle profiles for a rectangular object (indicated by green line) measured with centric phase encoding order. Note that a common legend for both graphs is shown in (a). [Color figure can be viewed in the online issue, which is available at wileyonlinelibrary.com.]

strongly different T_1 and T_2 contrast properties of CSF and brain tissue (transverse orientation, FOV = 320 × 190 mm^2, phase-encoding direction: left-right, imaging flip angle β = 7°, STEAM flip angle α = 60°, pixel bandwidth = 1250 Hz, slice thickness = 5 mm, in-plane resolution 3.3 mm, STEAM RF pulse shape = block shape, head SAR < 1.4 W/kg (<43%)). To study the impact of T_1, SENSE factors between 1 and 3 were applied, resulting in imaging shot durations between 209 and 79 ms, respectively. Moreover, to study the impact of T_2, three different echo timing schemes (FID first: TE = 1.7/2.5 ms, T_S= 4.2 ms; STE first: TE=1.7/2.5 ms, T_S= 4.2 ms; and STE* first: TE=1.7/2.5 ms, T_S= 0.8 ms) were compared, which resulted in a T_2 evolution time difference between the STE$^{(*)}$ and FID signals of 5 ms, 3.4 ms and 0 ms, respectively (cf. Eq. [3]).

RESULTS

Numerical Simulations

Figure 2 shows selected simulation results. The predicted STEAM flip angle α is shown as a function of the echo number in the pulse train for three different actual STEAM angles ($\alpha = 25°$, 50° and 75°), for two different actual imaging flip angles (β= 5° and 25°) and for two different longitudinal relaxation times ($T_1 = 200$ ms and 1000 ms, cf. Fig. 2a). Generally, an underestimation of the STEAM flip angle α is observed, which increases with increasing echo number and with decreasing T_1. This is due to the decay of the STEAM-prepared longitudinal magnetization and the recovery of the unprepared longitudinal magnetization caused by T_1 relaxation. For a moderate T_1 of 1000 ms, the resulting relative error is less than 1% for the first echo pair and up to 20% for the last echo pair in the pulse train. For a small T_1 of 200 ms, the resulting error is less than 5% for the first echo pair and up to 55% for the last echo pair. For all T_1 values, the relative error decreases with decreasing α. For small imaging flip angles (β =5°), the error increases monotonously with increasing echo number. In contrast, for large imaging flip angles (β =25°), the error shows an

oscillatory increase, which can be attributed to significant contributions from higher order coherences.

For a centric phase encoding order and the simple rectangular object considered in the simulations, the accuracy is essentially determined by the first echo pair of the pulse train (cf. Fig. 2b). However, the k-space weighting results in a degradation of the maps near the borders of the phantom. The oscillatory behavior observed for larger values of β during the pulse train did not lead to significant changes in the spatial flip angle profiles.

The results of the simulations confirm the preliminary results obtained in earlier studies (27), recommending an imaging pulse train with centric phase encoding order starting immediately after the STEAM preparation sequence to minimize T_1 effects. Moreover, to reduce potential accuracy degradations for more detailed anatomical structures (e.g. air-tissue interfaces) measured in the outer k-space regions, the acquisition train should be kept as short as possible. To reduce errors in the case of very short T_1, the upper limit of the working range could be reduced (e.g. to 50°) and the acquisition train could be further shortened using e.g. parallel imaging or k-space segmentation. The small impact of β on the accuracy of the method increases the robustness against inhomogeneous transmit fields, which also effect the imaging RF pulses.

Phantom Experiments

Figure 3a shows the predicted flip angle as a function of the reference flip angle for the oil phantom. Between 10° and 65° the absolute deviation from the reference flip angle is less than 1° and can be attributed to thermal noise in the underlying source images. Above 65° the flip angle is systematically underestimated, resulting in a flattening of the curve. This is in accordance with experiments reported for 3T (27) and may be mainly attributed to the relatively short T_1 of the oil phantom (cp. simulation results above). Below 10°, the flip angle is overestimated, which may be attributed to adverse error propagation for small flip angles (27).

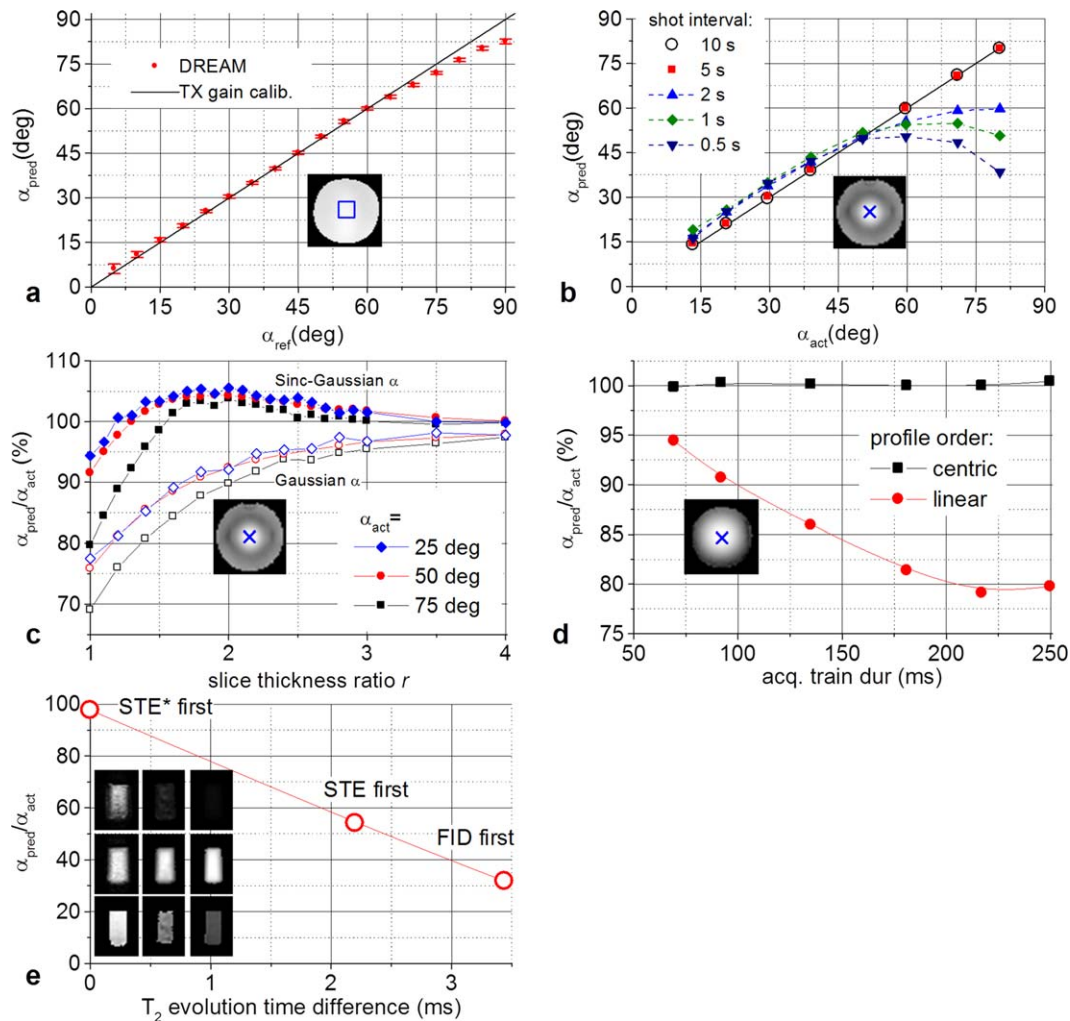Figure 3b shows the predicted flip angle as a function of the reference flip angle for different shot intervals. For

FIG. 3. DREAM B_1^+ mapping accuracy (phantoms). Graph (a) shows the predicted flip angle as a function of the nominal flip angle, which was considered as accurate reference for the employed oil phantom. The insert shows an underlying B_1^+ map along with a marker (blue square), indicating the ROI used for determining mean and standard deviation of the flip angle. Graph (b) shows the predicted flip angle as a function of the reference flip angle for different shot intervals. For short intervals (≤ 2 s), the ideal linear behavior is distorted. The insert shows an underlying B_1^+ map of the tap water phantom along with a marker (blue cross), indicating the location selected for evaluation. Graph (c) shows the predicted flip angle normalized to the reference flip angle as a function of the STEAM/imaging slice thickness ratio r for two different STEAM RF pulse shapes (sinc-gaussian and gaussian). For $r=1$ the flip angle is underestimated and approaches the correct value with increasing r. Note that for clarity the vertical axis starts at 65%. The insert shows an underlying B_1^+ map of the tap water phantom along with a marker (blue cross), indicating the location selected for evaluation. Graph (d) shows the normalized, predicted flip angle as a function of the acquisition train length for centric and linear phase encoding orders, respectively. While the systematic error is negligible for the centric order, the error is significant for the linear order and increases with increasing acquisition train length. Note that for clarity the vertical axis starts at 75%. The insert shows an underlying B_1^+ map of the spectroscopy phantom along with a marker (blue cross) indicating the location selected for evaluation. Graph (e) shows the normalized, predicted flip angle as a function of the STE/FID T_2-evolution time difference characteristic for the different timing schemes for a rubber phantom with very short T_2. The predicted angle is about 100% for "STE* first" and decreases strongly for "STE first" (65%) and "FID first" (30%). This is due to the increased T_2 decay of the STE signal as shown in the insert (top: STE, centre: FID, bottom B_1^+ map. From left to right: STE* first/STE first/FID first). [Color figure can be viewed in the online issue, which is available at wileyonlinelibrary.com.]

shot intervals ≥ 5 s, the data show an almost perfect linear behavior and predict flip angles between $10°$ and $80°$, which were considered as accurate reference and, hence, used to calibrate the abscissa by a global scale factor. For shot intervals ≤ 2 s, the predicted flip angles start to deviate from the linear behavior, leading to a strong degradation of the accuracy for very short shot intervals <1 s. Interestingly, the flip angle is underestimated

above about $50°$ and overestimated below this threshold. This can potentially be attributed to saturation and steady state effects, influencing and coupling the two longitudinal magnetization components used for B_1^+ encoding. The employed phantom fluid has a T_1 comparable to that of CSF. Hence, for brain B_1^+ mapping with DREAM, the acquisition delay between neighboring slices should be about five seconds or more to avoid
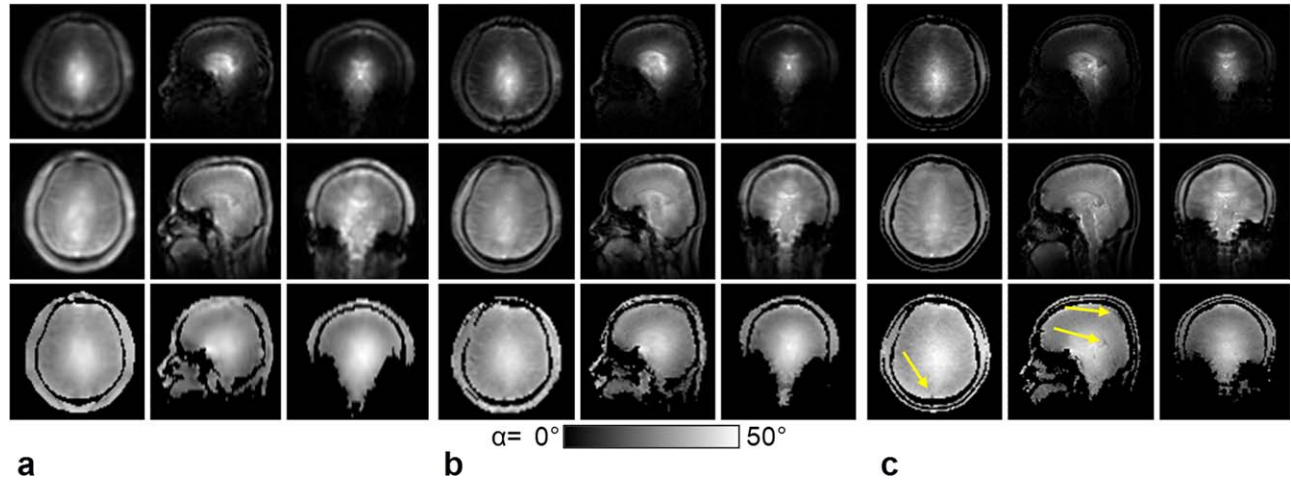
FIG. 4. Volumetric DREAM B_1^+ maps of the brain. Underlying images (top row: STE, middle row: FID) and resulting B_1^+ maps (bottom row: STEAM flip angle α) are shown for a selected volunteer. Three different isotropic resolutions are compared (a: 5 mm, b: 3.3 mm, c: 2.5 mm). The three orthogonal views reformatted from the isotropic data sets are shown (left column: transverse scan orientation, middle column: sagittal reformatting, right column: coronal reformatting). The scan times were (a) 8.1 s, (b) 9.9 s and (c) 21.5 s. The colored arrows (c, bottom) indicate slight flow artifacts in the arteries of the circle of Willis and in the great cerebral vein. [Color figure can be viewed in the online issue, which is available at wileyonlinelibrary.com.]

accuracy degradations caused by saturation effects, especially in the ventricle.

Figure 3c shows the normalized predicted flip angle as a function of the slice thickness ratio r. For $r = 1$, the flip angle is underestimated. For the standard sinc-Gaussian shaped STEAM RF pulses, the systematic error is about 6% for small flip angles (25°) and about 20% for large flip angles (75°). This may be explained by a spurious enhancement of the FID signal due to slice profile imperfections. In accordance with the experiments, a large impact on the B_1^+ mapping accuracy may be expected for flip angles near 90°, where the proper FID signal should vanish (cf. Eq. [1]). With increasing r, the predicted flip angle approaches the reference value in an overshooting manner. For $r = 2$, which is the chosen default value for the volumetric protocols, the flat plateau of the curve is reached and the residual error is smaller than 5%. For the gaussian STEAM pulses, the initial error is larger and the proper flip angle is approached in a slower, monotonous manner, resulting in a larger residual error of up to 10% for $r = 2$.

Figure 3d shows the predicted flip angle as a function of the acquisition train duration for the two applied phase encoding orders. For the centric order, the predicted angle is almost constant within the experimental error. Taking these values as accurate reference, the flip angle obtained from linear phase encoding order is underestimated by about 5% for a 70 ms acquisition train duration. Furthermore, the error increases up to 20% for 250 ms duration. These results are in very good qualitative agreement with the simulation results presented above (cf. Fig. 2).

Figure 3e shows the predicted flip angle as a function of the STE/FID T_2-evolution time difference characteristic for the different echo timing schemes. While a negligible deviation from the actual flip angle is observed for the "STE* first" option, strong deviations are observed for the "STE first" and "FID first" option. The underlying

images show that this is due to an enhanced signal decay of the stimulated echo for the phantom with ultrashort T_2. This result represents an experimental validation for the T_2-compensation of the "STE* first" option based on the virtual stimulated echo.

In Vivo Experiments

Figure 4 shows volumetric B_1^+ maps and underlying STE and FID images of the brain for one volunteer. The three orthogonal views (i.e. transverse, coronal, sagittal) reformatted from the isotropic data sets are shown for the three measured spatial resolutions (5 mm, 3.3 mm and 2.5 mm). The B_1^+ enhancement in the brain is well resolved at all spatial resolutions, and results in an actual B_1^+ between $\sim$60% and 125% of the nominal value in the central axial plane. This corresponds to a dynamic B_1^+ range of about two. The B_1^+ maps show good SNR even at 2.5 mm isotropic resolution, corresponding to a statistical error of less than 5% of the flip angle in the centre of the head. No saturation effects related to the odd/even scan order are visible in the reformatted coronal or sagittal views, which is in accordance with the phantom experiments.

Apparent B_1^+ drops are observed in the arteries of the circle of Willis or in the great cerebral vein. This may be attributed to flow artifacts, resulting from a flow-induced decay of the STE signal, which leads to an underestimation of the B_1^+.

Figure 5 shows volumetric B_1^+, B_0 and transceive phase maps including the underlying STE and FID images of another volunteer. The positions of the extremes of the transceive phase maps coincide well with the maxima of the B_1^+ maps in the centre of the head. The B_0 maps show the strongest off-resonance in the sagittal orientation with a shift of $\sim$900 Hz between the brain stem and the frontal lobe.

Figure 6 shows volumetric B_1^+ maps and underlying images measured in the presence of dielectric pads.
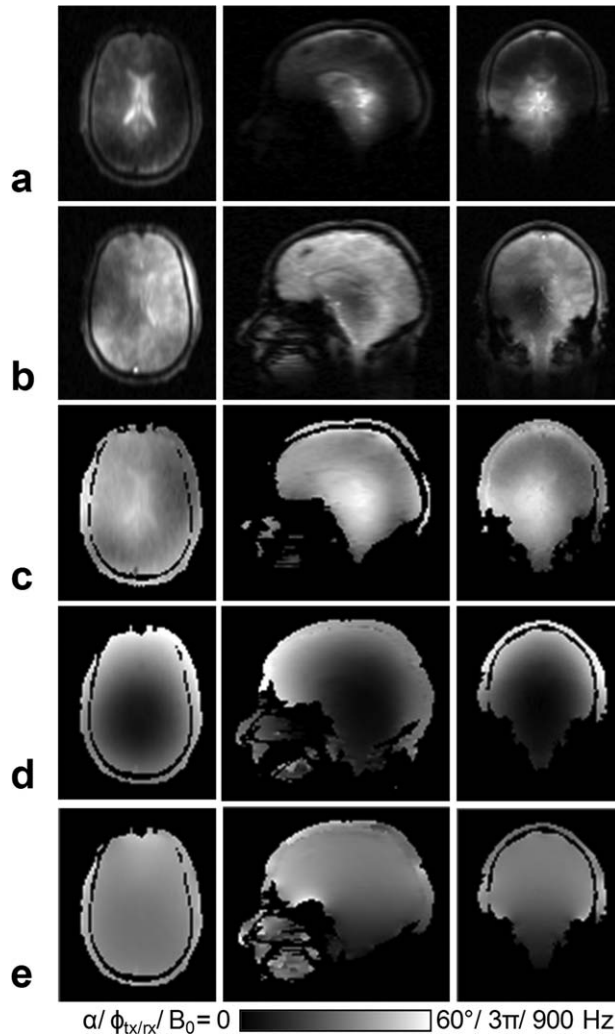
FIG. 5. Volumetric B_1^+, B_0, and transceive phase maps. Underlying DREAM images (a: STE, b: FID) and resulting maps (c: B_1^+ in terms of STEAM flip angle α, d: transceive phase $\varphi_{tx/rx}$, e: B_0 frequency shift, with the units given below the graph) are shown as reformatted images for a selected volunteer. The phase maps (d,e) were unwrapped. In the B_0 maps, the frequency shift between brain stem and frontal lobe is $\sim$900 Hz. Note the smoothness of the reformatted phase maps, indicating the robustness of the sequence against artifacts related to multislice acquisition.

Compared to normal quadrature excitation without pads, the B_1^+ is increased up to a factor of two near the pads, which results in a significant improvement in homogeneity in left/right direction for the selected volunteer.

Figure 7 shows volumetric B_1^+ maps and underlying images for single channel transmission. Compared to quadrature excitation, the two linearly polarized modes of the coils lead to a B_1^+ reduction of about 50% in the left/right and anterior/posterior regions of the central axial plane, respectively, for the selected volunteer.

For all volunteers, an increase of B_1^+ is observed in the proximity of the skullcap, which becomes particularly apparent in the coronal and sagittal reformatted views (cf. Figs. 4). Due to the T_2^* compensation of the sequence, this cannot be attributed to B_0 inhomogeneity related artifacts. However, a very similar effect has been
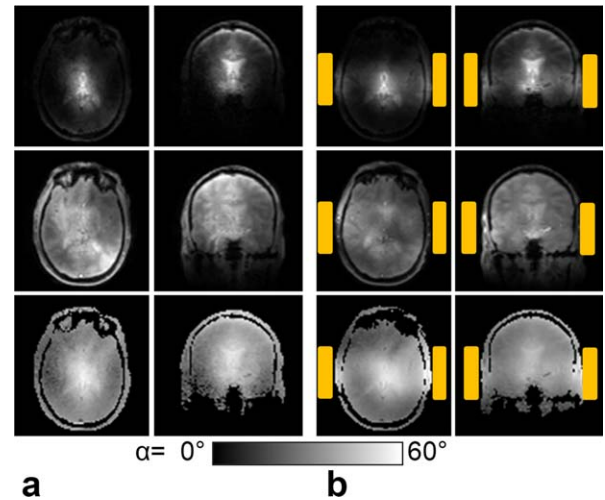

FIG. 6. RF excitation using dielectric pads. Underlying DREAM images (top row: STE, middle row: FID) and resulting B_1 maps (bottom row: STEAM flip angle α) are shown as reformatted images for a selected volunteer. Different excitation conditions are compared [without (a) and with (b) dielectric pads]. The position of the dielectric pads is schematically indicated by the colored slabs. Note the increased homogeneity in left–right direction between the pads. [Color figure can be viewed in the online issue, which is available at wileyonlinelibrary.com.]
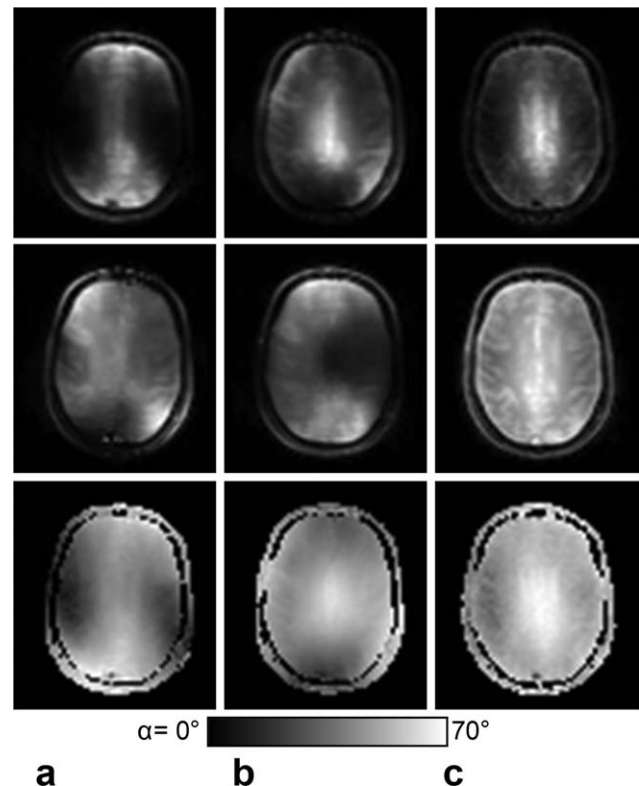

FIG. 7. RF excitation: different drive modes. Selected underlying DREAM images (top row: STE, middle row: FID) and resulting B_1^+ maps (bottom row: STEAM flip angle α) are shown for a selected volunteer. Different excitation conditions are compared (a: first transmit channel, b: second transmit channel, and c: quadrature excitation). The different transmit pattern of the two linearly polarized coil modes with transmit signal drops in anterior–posterior and left–right direction are well displayed.
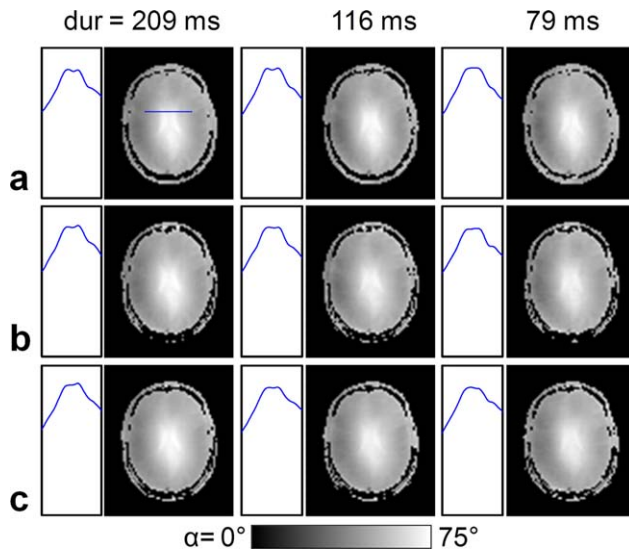
FIG. 8. DREAM B_1^+ maps of ventricle. B_1^+ maps of a transverse slice intersecting the ventricular system are shown for different timing schemes (a: FID first, b: STE first, c: STE* first) and acquisition train durations, corresponding to an increasing T_1-compensation from left to right and an increasing T_2-compensation from top to bottom (see Methods Section for details). In addition, 1D profiles of the B_1^+ maps selected along a line through the ventricle are shown (colored line). The ventricular system shows a small, but noticeable contrast, which reduces with increasing T_1- and T_2-compensation of the sequence. [Color figure can be viewed in the online issue, which is available at wileyonlinelibrary.com.]

predicted by Maxwell calculations for 7T using a human head model (36).

Figure 8 shows single-slice B_1^+ maps of the central axial plane measured with different echo timing schemes and different SENSE factors resulting in different acquisition train lengths. This corresponds to different degrees of T_2- and T_1-compensation of the sequence. Note that even for the highest SENSE factor ($= 3$), no backfolding artifacts are visible in the maps. The ventricular system shows a slight contrast, manifesting as a small, relative B_1^+ enhancement of the ventricle compared to the surrounding tissue ($\leq 4\%$). Due to the employed single-slice acquisition scheme, this cannot be attributed to saturation or slice profile effects. Also flow artifacts can be ruled out, because this would result in an apparent B_1^+ drop in the ventricle, similar to the effect observed in the large vessels (see above). Likewise, susceptibility effects are implausible because of the T_2^* compensation of the sequence. However, the ventricular contrast reduces with increasing T_1- and T_2-compensation and has almost disappeared for the STE*-first option combined with a short acquisition train length. Hence, the observed ventricular contrast may be predominantly attributed to small T_1- and T_2-relaxation effects.

DISCUSSION

In this work, a very fast, low-SAR MRI protocol based on the DREAM sequence has been compiled and optimized for B_1^+ mapping of the brain at 7T, allowing the acquisition of an image data set with isotropic 2.5 mm resolution in about 20 s. This is faster than corresponding B_1^+

mapping protocols based on e.g. AFI (21) or the Bloch-Siegert shift (26) by at least an order of magnitude. This acceleration is achieved by separating B_1^+ encoding from spatial encoding and by deriving the flip angle from two MR signals measured quasi-simultaneously. While the latter represents a unique property of the DREAM sequence, readout acceleration by separating B_1^+ encoding from spatial encoding is a quite general principle, which can be used for other B_1^+ mapping techniques as well, e.g. combining the double angle method with a saturation pre-pulse and spiral readout (19) or employing the stimulated echo with an EPI readout (20). In addition, the Bloch–Siegert shift has been used with a STEAM-based preparation sequence (37). Moreover, even a further acceleration of the DREAM approach using an EPI-type of readout is conceivable.

For the employed 32-channel coil array, isotropic resolutions in the range 2.5–5 mm with scan times between 20 and 8 s were found to be feasible for a volumetric brain B_1^+ mapping protocol based on DREAM. Higher resolutions were hampered by low SNR and longer scan time. For lower resolutions, the corresponding short scan time ($< 5s$) resulted in saturation-induced B_1^+ mapping artifacts especially for the ventricle due to its long T_1. This was caused by the overlapping slice acquisition order required for the volumetric multi-slice sequence, which could be avoided by applying appropriate slice-gaps or additional temporal delays (27).

However, owing to the high intrinsic SNR at 7T and the employed coil array, the 2.5 mm protocol was considered as a good compromise between spatial resolution, SNR and scan time. This tradeoff was facilitated by the usage of parallel imaging (31). The application of SENSE was straightforward and robust for the DREAM sequence, although it could be used only in one phase-encoding dimension. The propagation of SENSE artifacts caused by higher acceleration factors into the B_1^+ maps was weak.

For all DREAM protocols employed in vivo, the SAR was below 50% of the safety limits. For the standard "STE first" and "FID first" sequence options, SAR may be further reduced by about a factor of two without any scan time penalty by decreasing the peak B_1 of the STEAM RF pulses. Moreover, a further SAR reduction may be achieved by increasing the shot delays between the acquisition of subsequent slices. This is quite beneficial for ultra-high field MRI, where wave propagation effects may be strong and difficult to predict, and hence, a safety margin is highly desirable.

The stimulated echo is known to be flow sensitive (28). While the apparent B_1^+ drop at the great cerebral vein and the arteries of the circle of Willis could be attributed to flow artifacts easily, this mechanism cannot explain the small, but noticeable apparent B_1^+ enhancement of the ventricle. Qualitatively, this effect can be explained by an apparent B_1^+ reduction of the surrounding brain matter due to an increased T_1 or T_2 decay of the stimulated echo. This is supported by the experimental results obtained for different echo timing schemes and different image pulse train lengths.

The phantom experiments performed in this study show that the DREAM approach is relatively robust with respect to sequence parameter ranges. Moreover, the

approach consists of standard RF and gradient pulses, and hence, is easy to implement and to combine with other techniques such as e.g. parallel imaging or appropriate prepulses. In addition, the B_1^+ encoding principle is simple and intuitive, deriving the STEAM flip angle from the measured STE and FID signals by a simple analytical formula. Optimized RF pulses may further improve the STEAM slice profile (23), which could be particularly interesting for the tight timing used for the virtual stimulated echo STE*. This novel DREAM echo scheme represents an interesting option allowing both T_2/T_2^* compensation and adding new degrees of freedom to the method. Thus, sequence options acquiring all three signals STE*, FID, and STE are obvious.

The volumetric brain B_1^+ mapping protocols optimized for the present work could be transferred to higher (9.4T) or lower field strength (3T, 1.5 T) in a straightforward manner. Since fat-water partial volume effects are restricted to the scalp, no adaption of the echo times with respect to chemical shift encoding would be required for brain applications. However, the technique is not restricted to brain, and can be adapted to other anatomies as well. For lower field strengths, the smaller intrinsic SNR could be compensated by a lower SENSE factor, a longer signal sampling time or smaller ADC bandwidth, if necessary. Furthermore, the data acquisition can be segmented in k-space for applications where a higher spatial resolution is required.

The dynamic flip angle range of the DREAM sequence was found to be sufficient to cover the relatively strong B_1^+ variations occurring at 7T in the brain. This was even the case for single channel transmission, switching between the two linearly polarized modes of the head coil. Thus, in a parallel transmit experiment, e.g. an eight-channel volumetric B_1^+ calibration scan with 5 mm isotropic resolution could be measured in about a minute. In addition, the dynamic range could be further improved by using the individual transmit channels, or appropriate superpositions (38), for B_1^+ encoding (i.e. for the STEAM RF pulses) and the full transmit matrix for the imaging RF pulses (39).

The volumetric DREAM B_1^+ maps may also be used to support SAR calculations (8,9) or Electric Properties Tomography (EPT) to improve safety and deliver new diagnostic information for e.g. glioma patients (8). These applications would benefit from the relatively high spatial resolution and from the volumetric transceive phase map delivered for free. Furthermore, the volumetric B_0 phase map delivered as DREAM by-product could be used for higher-order B_0 shimming and could therefore represent a useful add-on for a number of applications.

In conclusion, DREAM enables very fast and safe B_1^+ mapping at ultrahigh fields. It has been shown to be a simple and robust approach with the potential to support both conventional and parallel transmit applications at very high fields.

REFERENCES

1. van der Kolk AG, Hendrikse J, Zwanenburg JJ, Visser F, Luijten PR. Clinical applications of 7T MRI in the brain. Eur J Radiol 2011 [Epub ahead of print].

2. Saekho S, Yip CY, Noll DC, Boada FE, Stenger VA. Fast-kz three-dimensional tailored radiofrequency pulse for reduced B1 inhomogeneity. Magn Reson Med 2006;55:719–724.

3. Hoult DI, Phil D. Sensitivity and power deposition in a high-field imaging experiment. J Magn Reson Imaging 2000;12:46–67.

4. Ibrahim TS, Lee R, Baertlein BA, Abduljalil AM, Zhu H, Robitaille PM. Effect of RF coil excitation on field inhomogeneity at ultra high fields: a field optimized TEM resonator. Magn Reson Imaging 2001;19:1339–1347.

5. Katscher U, Börnert P, Leussler C, van den Brink JS. Transmit SENSE. Magn Reson Med 2003;49:144-150.

6. Zhu Y. Parallel excitation with an array of transmit coils. Magn Reson Med 2004;51:775–784.

7. Venkatesan R, Lin W, Haacke EM. Accurate determination of spin-density and T1 in the presence of RF-field inhomogeneities and flip-angle miscalibration. Magn Reson Med 1998;40:592–602.

8. Katscher U, Voigt T, Findeklee C, Vernickel P, Nehrke K, Dössel O. Determination of electric conductivity and local SAR via B1 mapping. IEEE Trans Med Imaging 2009;28:1365-1374.

9. Katscher U, Findeklee C, Voigt T. B_1-based specific energy absorption rate determination for nonquadrature radiofrequency excitation. Magn Reson Med 2012;68:1911–1918.

10. van der Meulen P, van Yperen GH. A novel method for rapid pulse angle optimisation. In Proceedings of the 5th Annual Meeting of SMRM, Montral, Canada, 1986, abstract 1129.

11. Carlson JW, Kramer DM. Rapid radiofrequency calibration in MRI. Magn Reson Med 1990;15:438–445.

12. Klose U. Mapping of the radio frequency magnetic field with a MR snapshot FLASH technique. Med Phys 1992;19:1099–1104.

13. Insko E, Bolinger L. Mapping of the radio frequency field. J Magn Reson Ser A 1993;103:82–85.

14. Akoka S, Franconi F, Seguin F, Le Pape A. Radiofrequency map of an NMR coil by imaging. Magn Reson Imaging 1993;11:437–441.

15. Stollberger R, Wach P. Imaging of the active B1 field in vivo. Magn Reson Med 1996;35:246–251.

16. Sled JG, Pike GB. Correction for B_1 and B_0 variations in quantitative T_2 measurements using MRI. Magn Reson Med 2000;43:589–593.

17. Fernandez-Seara MA, Song HK, Wehrli FW. Trabecular bone volume fraction mapping by low-resolution MRI. Magn Reson Med 2001;46:103–113.

18. Wang J, Qiu M, Constable RT. In vivo method for correcting transmit/receive nonuniformities with phased array coils. Magn Reson Med 2005;53:666–674.

19. Cunningham CH, Pauly JM, Nayak KS. Saturated double-angle method for rapid B_1 mapping. Magn Reson Med 2006;55:1326–1333.

20. Jiru F, Klose U. Fast 3D radiofrequency field mapping using echoplanar imaging. Magn Reson Med 2006;56:1375–1379.

21. Yarnykh VL. Actual flip-angle imaging in the pulsed steady state: a method for rapid three-dimensional mapping of the transmitted radiofrequency field. Magn Reson Med 2007;57:192–200.

22. Helms G, Finsterbusch J, Weiskopf N, Dechent P. Rapid radiofrequency field mapping in vivo using single-shot STEAM MRI. Magn Reson Med 2008;60:739–743.

23. Volz S, Nöth U, Rotarska-Jagiela A, Deichmann R. A fast B 1–mapping method for the correction and normalization of magnetization transfer ratio maps at 3 T. Neuroimage 2010;49:3015–3026.

24. Chung S, Kim D, Breton E, Axel L. Rapid B_1^+ mapping using a preconditioning RF pulse with TurboFLASH readout. Magn Reson Med 2010;64:439–446.

25. Morrell GR. A phase-sensitive method of flip angle mapping. Magn Reson Med 2008;60:889–894.

26. Sacolick LI, Wiesinger F, Hancu I, Vogel MW. B1 mapping by Bloch-Siegert shift. Magn Reson Med 2010;63:1315–1322.

27. Nehrke K, Börnert P. DREAM-a novel approach for robust, ultrafast, multislice B(1) mapping. Magn Reson Med 2012;68:1517–1526.

28. Frahm J, Haase A, Matthai KD, Merboldt KD, Hänicke W. Rapid NMR imaging using stimulated echoes. J Magn Reson 1985;65:130–135.

29. Woessner DE. Effects of diffusion in nuclear magnetic resonance spin-echo experiments. J Chem Phys 1961;34:2057–2061.

30. Hennig J. Echoes: how to generate, recognise, use or avoid them in MR imaging sequences. Concepts Magn Reson 1991;3:125–143.

31. Pruessmann KP, Weiger M, Scheidegger MB, Boesiger P. SENSE: sensitivity encoding for fast MRI. Magn Reson Med 1999;42:952–962.

32. Rahmer J, Börnert P, Groen J, Bos C. Three-dimensional radial ultra-short echo-time imaging with T2 adapted sampling. Magn Reson Med 2006;55:1075–1082.

33. Herraez MA, Gdeisat MA, Burton DR, Lalor MJ. Robust, fast, and effective two-dimensional automatic phase unwrapping algorithm based on image decomposition. Appl Opt 2002;41:7445–7455.

34. Haines K, Smith N, Webb A. New high dielectric constant materials for tailoring the B_1^+ distribution at high magnetic fields. J Magn Reson 2010;203:323–327.

35. Teeuwisse W, Brink W, Haines K, Webb A. Simulations of high permittivity materials for 7 T neuroimaging and evaluation of a new barium titanate-based dielectric. Magn Reson Med 2012;67:912–918.

36. Vaughan JT, Garwood M, Collins CM, Liu W, DelaBarre L, Adriany G, Andersen P, Merkle H, Goebel R, Smith MB, Ugurbil K. 7T vs. 4T: RF power, homogeneity, and signal-to-noise comparison in head images. Magn Reson Med 2001;46:24–30.

37. Nehrke K, Börnert P. Fast B_1 mapping using a STEAM-based Bloch-Siegert preparation pulse. In Proceedings of the 19th Annual Meeting of ISMRM, Montreal, Canada, 2011. p. 4411.

38. Nehrke K, Börnert P. Eigenmode analysis of transmit coil array for tailored B_1 mapping. Magn Reson Med 2010;63:754–764.

39. Khalighi MM, Sacolick LI, Rutt BK. Signal to noise ratio analysis of Bloch-Siegert B_1 mapping. In Proceedings of the 18th Annual Meeting of ISMRM, Stockholm, Sweden, 2010. p. 2842.